


Thermally Polarized Solid-State Spin Sensor

Reginald Wilcox^{1,2}, Erik Eisenach^{1,2}, John Barry^{2,*}, Matthew Steinecker², Michael O’Keeffe², Dirk Englund¹, and Danielle Braje²

¹*Massachusetts Institute of Technology, Cambridge, Massachusetts 02139, USA*

²*MIT Lincoln Laboratory, Lexington, Massachusetts 02421, USA*

 (Received 7 September 2021; revised 20 January 2022; accepted 2 March 2022; published 4 April 2022)

Quantum sensors based on spin defect ensembles have seen rapid development in recent years, with a wide array of target applications. Historically, these sensors have used optical methods to prepare or read out quantum states. However, these methods are limited to optically polarizable spin defects, and the spin ensemble size is typically limited by the available optical power or acceptable optical heat load. We demonstrate a solid-state sensor employing a nonoptical state preparation technique, which harnesses thermal population imbalances induced by the defects’ zero-field splitting. Readout is performed using the recently demonstrated microwave cavity readout technique, resulting in a sensor architecture that is entirely nonoptical and broadly applicable to all solid-state paramagnetic defects with a zero-field splitting. The implementation in this work uses Cr^{3+} defects in a sapphire (Al_2O_3) crystal and a simple microwave architecture where the host crystal also serves as the high quality-factor resonator. This approach yields a near-unity filling factor and high single-spin-photon coupling, producing a broadband magnetometer with a minimum sensitivity of $9.7 \text{ pT}/\sqrt{\text{Hz}}$ near 5 kHz.

DOI: [10.1103/PhysRevApplied.17.044004](https://doi.org/10.1103/PhysRevApplied.17.044004)

I. INTRODUCTION

Solid-state spin systems have transitioned from physics demonstrations to promising quantum sensors [1–16] as performance has improved through materials engineering [17–25], coherent control [26–35], and enhanced readout [36–43]. For magnetometry, solid-state sensor performance has progressed rapidly enough that sensitivity rivaling that of legacy sensors may soon be within reach [44–49]. Moreover, when factors such as bandwidth, dynamic range, or portability are considered, solid-state quantum sensors may offer performance for select applications that cannot be matched by existing sensors [48]. For example, superconducting quantum interference devices [50] offer sensitivities below $10 \text{ fT}/\sqrt{\text{Hz}}$ but are cryogenic, limiting their portability, while vapor cell magnetometers can provide sensitivities below $1 \text{ fT}/\sqrt{\text{Hz}}$ [51] in magnetically shielded environments, but performance suffers in magnetic field gradients, and only scalar implementations operate natively in Earth’s magnetic field. Meanwhile, classical sensors such as fluxgates and search coils offer sensitivities near $1 \text{ pT}/\sqrt{\text{Hz}}$ and $1 \text{ fT}/\sqrt{\text{Hz}}$, respectively, but have limited bandwidth or dynamic range and may be bulky [52].

Whether measuring electromagnetic fields, temperature, or time [49,53–60], spin sensors perform three primary processes [44,49]: quantum state initialization, interaction with the environment, and readout. Initialization has seen little recent development and is nearly universally achieved optically [22]. This limits solid-state sensing species to optically polarizable defects, with the bulk of experimental effort dedicated to nitrogen-vacancy (N-V) diamond [17]. Moreover, the light source is often the primary driver of device complexity and power consumption. To overcome these limitations, we introduce a quantum sensor using chromium ions (Cr^{3+}) in sapphire (also known as ruby).

The key advance of this work is combining initialization and readout techniques to enable a simple sensor architecture with compelling performance. The sensor employs entirely passive initialization at room temperature. This initialization is produced by thermalization of the defects’ spin states, which differ in energy by the zero-field-splitting (ZFS). In addition, the sensor extends the recently demonstrated microwave (MW) cavity readout technique [38,39] to a room-temperature, non-N-V diamond system. Together, these advances result in an entirely MW-based (nonoptical) device that exhibits high sensitivities when used as a magnetometer. More broadly, this work serves as proof of concept for a wide variety of sensing modalities employing diverse solid-state defects, which need not be optically polarizable.

*john.barry@ll.mit.edu

II. THERMAL SPIN POLARIZATION IN RUBY

In contrast to optically polarized sensors, the device demonstrated here is passively initialized through thermalization of the spin states of the paramagnetic defects. A system in thermal equilibrium will preferentially populate lower-energy states according to the Boltzmann distribution. For paramagnetic defects with a ZFS, an energy difference between spin states is induced by the crystalline electric field, passively creating a population imbalance in a process we refer to as thermal spin polarization. The Cr^{3+} ions in ruby have spin $S = \frac{3}{2}$ and exhibit a $2\pi \times 11.5$ GHz ZFS between the $|m_s = +\frac{3}{2}\rangle$ and $|m_s = +\frac{1}{2}\rangle$ states [61]. At 293 K, the net population difference between these two states in thermal equilibrium is 0.047% of the total number of Cr^{3+} ions, corresponding to a polarized spin density of approximately $7 \times 10^{15} \text{ cm}^{-3}$ (see Sec. S4 in the Supplemental Material [62]). We note that thermal spin polarization is also employed, for example, in electron paramagnetic resonance spectroscopy or in demonstrations of cavity quantum electrodynamic effects, but crucially the energy difference in such experiments is typically produced by strong magnetic fields rather than by an intrinsic property of the system [63–65]. To achieve similar polarization to that induced in ruby, systems without a ZFS would require a large magnetic field of 0.2 T [66]. In contrast, only a small field of approximately 0.003 T is applied in this device, sufficient to lift undesirable degeneracies but with negligible impact on spin polarization.

Ruby has several key properties which make it well suited as a host crystal for MW cavity readout. First, the ruby crystal can serve as the dielectric resonator, which vastly improves the filling factor over volume-limited crystals such as N-V diamond coupled to an external resonator. Second, the ruby resonator supports a high quality-factor mode (approximately 50 000) near the spin transition frequency [67] enabling a large single-spin-photon coupling. Third, ruby crystal growth is a mature technology, with high-purity single-crystal material available in liter-scale volumes [68,69]. Finally, ruby's anisotropy induces sufficient thermal spin polarization for high-sensitivity magnetometry at room temperature. Together, these properties allow creation of a quantum sensor free of lasers, large magnetic fields, and cryogenics. Because the sensing head has a volume less than 100 cm^3 and the supporting rf and readout electronics are commercially available, this sensor architecture may be viable for select nonlaboratory applications such as time-domain electromagnetic surveying.

III. THEORETICAL BACKGROUND

To describe the use of ruby as a magnetometer, we begin by reviewing the ruby Hamiltonian under application of an external magnetic field $\mathbf{B} = [B_x, B_y, B_z]$. With the z axis

defined parallel to the ruby c -axis, the Cr^{3+} ground-state Hamiltonian is [61]

$$\mathcal{H} = g_{\parallel} \mu_B B_z S_z + g_{\perp} \mu_B (S_x B_x + S_y B_y) + D [S_z^2 - \frac{1}{3} S(S+1)], \quad (1)$$

where μ_B is the Bohr magneton, g_{\parallel} and g_{\perp} are the axial and transverse g -factors, and D is the ZFS parameter. The total spin angular momentum is $S = \frac{3}{2}$, and S_x , S_y , and S_z are the spin matrices. At room temperature, the ZFS is $2D \approx -2\pi \times 11.49$ GHz, and $g_{\parallel} \approx g_{\perp} \approx 2$ [61]. All Cr^{3+} sites are magnetically equivalent.

Without an applied magnetic field, the eigenstates form a Kramers doublet with degenerate pairs $|m_s = \pm\frac{1}{2}\rangle$ and $|m_s = \pm\frac{3}{2}\rangle$ [70]. For magnetic fields applied parallel to the c -axis, the eigenenergies vary linearly with $S_z B_z$, as shown in Fig. 1(a) [61]. In this work, we primarily consider magnetic fields parallel to the c -axis (see Sec. S1 in the Supplemental Material [62]). If the eigenenergies are accurately measured, their magnetic field dependence can be exploited for high-sensitivity magnetometry.

Microwave cavity readout interrogates the spin transition frequency ω_s by applying a MW probe signal at frequency ω_d to the ruby resonator and measuring the reflected signal [38]. Shifts in ω_s are encoded in the spin ensemble's absorptive and dispersive modification of the reflection coefficient Γ . The complex-valued voltage reflection coefficient is [38]

$$\Gamma = -1 + \frac{\kappa_{c1}}{\frac{\kappa_c}{2} + i(\omega_d - \omega_c) + \Pi}, \quad (2)$$

where $\kappa_c \equiv \kappa_{c0} + \kappa_{c1}$ is the loaded cavity linewidth, κ_{c0} and κ_{c1} are the intrinsic cavity linewidth and input couplings rates, ω_c is the bare cavity resonance, and Π is an interaction term incorporating the absorptive and dispersive effects of the spins on the ruby resonator. The interaction term Π may be written as [38]

$$\Pi = \frac{g_s^2 N}{\frac{\kappa_s}{2} + i(\omega_d - \omega_s) + \frac{g_s^2 n_{\text{cav}} \kappa_s / (2\kappa_{\text{th}})}{\frac{\kappa_s}{2} - i(\omega_d - \omega_s)}}, \quad (3)$$

where $\kappa_s = 2/T_2$ is the homogeneous width of the spin resonance (see Sec. S2 in the Supplemental Material [62]), $\kappa_{\text{th}} = 1/T_1$ is the thermal polarization rate, n_{cav} is the average number of MW photons in the cavity over the cavity lifetime $1/\kappa_c$, and N is effective number of polarized spins, given by the population difference between the $|m_s = +\frac{3}{2}\rangle$ and $|m_s = +\frac{1}{2}\rangle$ states. The single spin-photon coupling is $g_s = \gamma n_{\perp} / 2\sqrt{\hbar\omega_c \mu_0 / V_{\text{cav}}}$, where γ is the electron gyromagnetic ratio, V_{cav} is the ruby resonator modal field volume, μ_0 is the vacuum permeability, and $0 \leq n_{\perp} \leq 1$ is a geometric factor, which occurs because

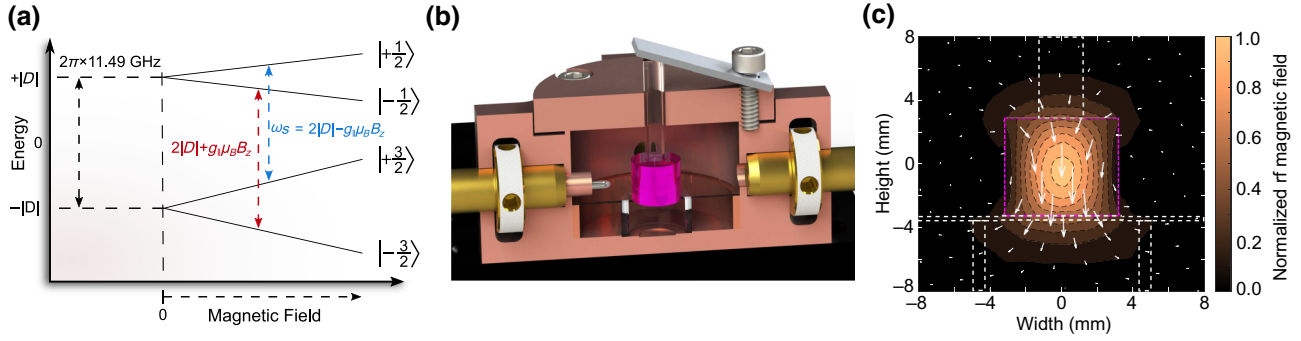


FIG. 1. Ruby resonator design. (a) The electronic ground state of trivalent chromium (Cr^{3+}) in sapphire consists of two pairs of degenerate spin doublets separated by a $2\pi \times 11.49$ GHz zero-field splitting. External magnetic fields applied along the crystallographic c -axis lift the degeneracy of the $|m_s = \pm\frac{1}{2}\rangle$ and $|m_s = \pm\frac{3}{2}\rangle$ sublevels as shown, allowing the $|m_s = +\frac{3}{2}\rangle \leftrightarrow |m_s = +\frac{1}{2}\rangle$ transition with frequency ω_s to be addressed spectroscopically. (b) Device cross section. Microwaves are coupled into the ruby resonator shown in pink, with a single probe loop on the left. While the shield supports up to four probe loops, only a single probe is used in this work. The ruby resonator is centered on a semi-insulating wafer of silicon carbide (SiC) and is clamped in place by a spring-loaded fused-silica tube. A copper shield encloses the ruby resonator and improves the resonator's quality-factor by decreasing radiative losses. (c) Simulated rf magnetic field distribution of the ruby resonator's $\text{TE}_{01\delta}$ mode. The rf magnetic field is denoted by white arrows, the ruby resonator is outlined in pink, and the SiC and fused-silica support structures are indicated by white dashed lines.

only fields transverse to the spin quantization axis can drive transitions. The reflection coefficient Γ is maximally sensitive to changes in magnetic field when all frequencies are equal: $\omega_c = \omega_d = \omega_s$. By measuring the reflection coefficient for various values of ω_s , ω_d , and applied MW power, the spin-cavity interaction can be characterized. Such characterization allows straightforward optimization of the device as a magnetometer.

IV. EXPERIMENTAL SETUP

A. Microwave cavity

Previous room-temperature spin-cavity coupling experiments employed a solid-state spin system coupled to an external MW cavity [38,39,71,72]. In this work, the MW cavity is formed by the host crystal of the spin system itself. A monocrystalline ruby sample with a Cr^{3+} concentration of 0.05% by weight (see Sec. S4 in the Supplemental Material [62]) is used to produce a $\text{TE}_{01\delta}$ cavity mode near the Cr^{3+} spin resonance. The resulting ruby resonator is a cylinder 5.85 mm tall and 6.98 mm in diameter [73], with the c -axis oriented radially. With the given dimensions and relative dielectric constants of $\epsilon_{\parallel} = 11.5$ and $\epsilon_{\perp} = 9.4$ (parallel and perpendicular to the c -axis, respectively) [73–75], the ruby resonator exhibits a $\text{TE}_{01\delta}$ resonance [Fig. 1(c)] at $\omega_c \approx 2\pi \times 11.4$ GHz with a filling factor $\zeta \approx 0.7$ (see Sec. S3 in the Supplemental Material [62]). As constructed, the ruby resonator has an unloaded quality factor of $Q_0 = 35\,000$ [76].

The resonator is centered coaxially in a cylindrical copper shield with an inner height of 16.1 mm and an inner diameter of 24 mm [73], as shown in Fig. 1(b). This thin shield (5 mm) improves the quality factor by mitigating

radiative losses at 11.4 GHz, but does not significantly disturb dc and low-frequency magnetic fields of interest. The ruby resonator is supported mechanically by a 330- μm -thick silicon carbide (SiC) wafer and a spring-loaded fused-silica tube. By providing a strong thermal link to the copper shield, the SiC reduces temperature fluctuations due to the MW-induced heat load on the crystal, thereby decreasing temperature-dependent shifts in the cavity resonance [77].

The shielded ruby resonator is placed in a uniform magnetic field \mathbf{B}_0 created by an electromagnet, which is driven by a bipolar operational amplifier power supply. The field is oriented along the c -axis of the ruby resonator. This bias magnetic field lifts the degeneracy of the $|m_s = \pm\frac{1}{2}\rangle$ and $|m_s = \pm\frac{3}{2}\rangle$ spin states, allowing the $|m_s = +\frac{1}{2}\rangle \leftrightarrow |m_s = +\frac{3}{2}\rangle$ transition (with angular frequency ω_s) to be addressed spectroscopically as an effective two-level system [78]. For magnetometry data in this work, $B_0 \approx 31$ G is chosen so that the spin resonance at ω_s and cavity resonance at ω_c are nearly equal. The Zeeman splitting from B_0 is small compared to the ZFS and does not contribute appreciably to spin polarization. The probe MWs, at angular frequency ω_d , are then tuned so $\omega_d \approx \omega_c \approx \omega_s$ to maximize the spin-cavity interaction.

B. Microwave signal chain

In the MW cavity readout technique, the spin resonance frequency ω_s is inferred from the ensemble's dispersive shift of the cavity resonance [38,39]. The implementation in this work interrogates the cavity resonance using a homodyne receiver structure, as shown in Fig. 2. The probe MWs are first split into a signal arm and a reference arm. Next, the signal arm is attenuated as needed, sampled by

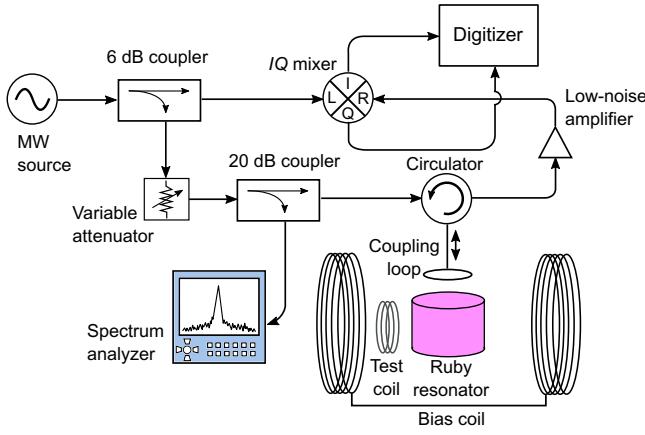


FIG. 2. Experimental setup and MW signal chain. A probe MW signal near-resonant with the ruby resonator is split using a 6 dB directional coupler into a signal arm and a reference arm. Incident microwaves in the signal arm probe the ruby resonator through a circulator. MW signals exiting the circulator are then amplified by a low-noise amplifier and mixed to baseband using an IQ mixer. The spectrum analyzer monitors the MW power incident on the ruby resonator.

a spectrum analyzer through a 20-dB directional coupler, and delivered to a circulator. Microwaves out of the circulator are coupled into the ruby resonator using a probe loop inserted into the copper shield. By using a circulator, incident MWs are isolated from those reflected by the resonator, allowing the complex reflection coefficient Γ to be measured. A 24-dB-gain low-noise amplifier amplifies the reflected MWs, which are terminated in an IQ mixer's rf port. The IQ mixer's LO port is driven by the reference arm.

The signal is downconverted to baseband by the IQ mixer, and both the I and Q channels are digitized. Capturing both the I and Q mixer channels allows the reflected signal to be reconstructed in software as if there were a physical phase shifter (see Sec. S8 in the Supplemental Material [62]). The software reconstruction separates the signal into an absorptive channel and a dispersive channel.

V. EXPERIMENTAL RESULTS

A. Spin-cavity interaction

To quantify the strength of the interaction between the cavity and spin ensemble, a low-power MW signal is applied to the ruby resonator. The reflection coefficient is measured as the MW drive frequency ω_d and the magnetic bias field (and thus the spin resonance frequency ω_s) are independently varied [79]. Figure 3 depicts the observed and simulated avoided crossing with 0 dBm applied to the ruby resonator. The best fit parameters derived from Eqs. (2) and (3) are $\kappa_c = 2\pi \times 660$ kHz, $\kappa_s = 2\pi \times 42$ MHz, $\kappa_{th} = 2\pi \times 120$ kHz, and $g_{\text{eff}} \equiv g_s \sqrt{N} = 2\pi \times 3.5$ MHz,

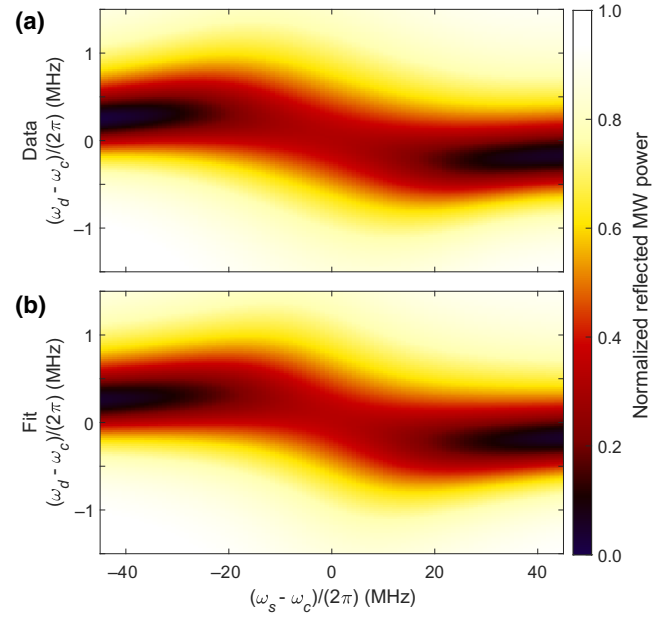


FIG. 3. Ensemble-cavity coupling. (a) The spin resonance frequency is swept across the bare cavity resonance (horizontal axis) by varying the bias magnetic field; by concurrently varying the MW drive frequency (vertical axis), an avoided crossing due to the ensemble-resonator coupling is observed. (b) Simulation accurately reproduces experimental results, providing best-fit system parameters as described in the main text. Data were recorded with 0 dBm applied to the ruby resonator under critical coupling, and the reflection coefficient is normalized to unity.

giving $N = 3.5 \times 10^{14}$ polarized Cr^{3+} spins with the calculated value $g_s = 2\pi \times 0.2$ Hz (see Sec. S6 in the Supplemental Material [62]). As this value for g_s corresponds to the coupling strength at the center of the resonator, the parameter N represents an effective number of polarized spins coupled, if each spin were coupled with identical coupling strength. Using the Cr^{3+} concentration, we compute $N_{\text{tot}} = 8 \times 10^{17}$ Cr^{3+} spins present within the modal field volume. This corresponds to an effective polarization of $\mathcal{P} = 0.044\%$, in agreement with the expected value (see Sec. S4 in the Supplemental Material [62]). The collective cooperativity, defined as $\xi = 4g_{\text{eff}}^2/(\kappa_s \kappa_c)$, is a dimensionless figure of merit describing the strength of the ensemble-cavity interaction [80]. The given fit parameters result in a collective cooperativity of $\xi = 1.8$, indicating operation in the high-cooperativity regime ($\xi > 1$).

To characterize the system's performance as a magnetometer, the system is probed under optimal applied MW power (see Sec. S7 in the Supplemental Material [62]). The cavity interaction with probe MWs is observed by fixing the bias magnetic field so that $\omega_s \approx \omega_c$ and then sweeping the MW drive frequency ω_d and monitoring the reflected signal, seen in Fig. 4(a). This is used to properly center

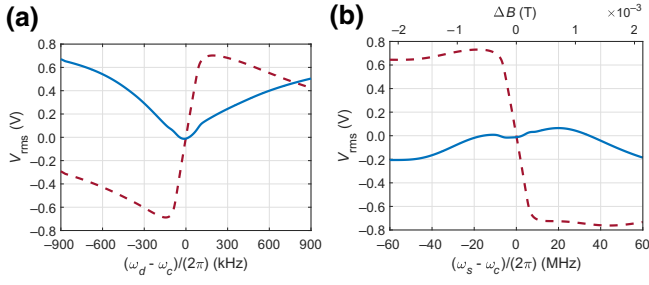


FIG. 4. Reflection measurements of the spin-cavity response. (a) Reflected absorptive (—) and dispersive (---) voltage signal as a function of drive-cavity detuning ($\omega_d - \omega_c$). The dispersive shift is near-linear around the zero-crossing. The asymmetry in the cavity reflection profile is due to nonmonotonic amplifier gain near saturation. (b) Reflected absorptive (—) and dispersive (---) voltage signal as a function of spin-cavity detuning ($\omega_s - \omega_c$). Magnetometry is performed in the linear region near zero detuning. The maximum slope on the dispersive component, $M_{\max} \approx 3000$ V/T, sets the device’s response when operated as a magnetometer. This maximum slope region extends ± 0.25 mT around zero detuning, which approximately sets the sensor’s dynamic range. The slight observed asymmetry in both components is hypothesized to result from the off-resonant spin transition interacting with the ruby resonator mode and imperfect alignment of the bias field with the optical axis (less than approximately 10°). The applied MW power for both panels is 11 dBm.

the drive frequency for magnetometry and reveals the cavity linewidth κ_c , which is monitored to adjust the probe loop for critical coupling. The dispersive and absorptive responses of the spin resonance are observed by fixing the MW drive frequency so that $\omega_d \approx \omega_c$ and sweeping the bias magnetic field, seen in Fig. 4(b). (Iterating between sweeps of ω_d and ω_s allows these parameters to be accurately set to ω_c .) When the spin transitions are resonant with the cavity, the dispersive component exhibits a sharp slope with maximum value $M_{\max} \approx 3000$ V/T. This regime is of particular interest to magnetometry as the reflected MW signal is maximally sensitive to changes in the magnetic field [38].

B. Magnetometry

Small changes in the external magnetic field may be detected by monitoring the dispersive shift of the reflected MW probe signal. For high-sensitivity magnetometry, the bias magnetic field is chosen so that the device operates in the region of maximal slope M_{\max} where the reflected signal is most sensitive to the applied magnetic field. Magnetometry measurements are performed using an independently applied ac test magnetic field. The chosen field magnitude is small compared to the spin resonance linewidth κ_s so as not to perturb the system from the optimal configuration. A low-noise signal generator drives a coil to generate a test field with amplitude $B_{\text{test}}^{\text{rms}} = 242$ nT, frequency $\omega_m = 2\pi \times 10$ Hz, and orientation along the

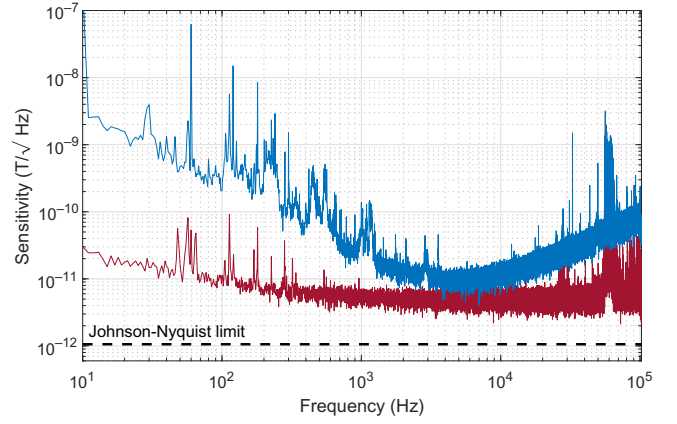


FIG. 5. Broadband magnetometry using Cr^{3+} ions in ruby. Magnetometry is performed by measuring MWs reflected off the ruby resonator using an IQ mixer. Based on the noise spectral density measured during magnetometer operation (—) we project a sensitivity of approximately 10 pT/ $\sqrt{\text{Hz}}$ in the low-noise band between 4 kHz and 6 kHz. The projected sensitivity in the low-noise band approaches the noise floor set by amplifier, mixer, and readout electronics (---). We compute a thermal-noise-limited sensitivity (---) of 1.1 pT/ $\sqrt{\text{Hz}}$ using the measured device response from Fig. 4(b). See Sec. S9 in the Supplemental Material [62] for a discussion of the noise spectrum shape.

ruby c -axis. This frequency is chosen high enough that flicker noise does not limit the digitization fidelity, but low enough that the test field is not significantly attenuated by the copper shield (see Sec. S5 in the Supplemental Material [62]). The amplitude of the applied test field is verified using three independent methods (see Sec. S5 in the Supplemental Material [62]).

By computing the spectrum of the rms voltage in the dispersive channel and evaluating the peak at the test field frequency ω_m , which we denote V_m , we can calculate the projected magnetic sensitivity as

$$\eta = \frac{e_n}{V_m/B_{\text{test}}^{\text{rms}}}, \quad (4)$$

where e_n is the rms voltage noise floor of the single-sided spectrum and $B_{\text{test}}^{\text{rms}}$ is the rms amplitude of the applied test field. There are competing effects which dictate the optimal interrogation MW power. Increasing the MW power increases the signal amplitude, but also causes power broadening, decreasing the fractional change in signal for a given change in applied magnetic field [81]. For magnetometry, the device is operated at the optimized values of 11 dBm of MW power and a bias field of $B_0 = 31$ G (see Sec. S7 in the Supplemental Material [62]). This bias field B_0 produces $\omega_s \approx \omega_c$, consistent with the expectation that $\omega_s \approx \omega_c \approx \omega_d$ is optimal for magnetometry [38,61].

We measure a noise floor of $e_n = 26$ nV/ $\sqrt{\text{Hz}}$ at the digitizer under optimal operating conditions. From this measurement, we project an optimal sensitivity of

$\eta = 9.7 \text{ pT}/\sqrt{\text{Hz}}$ at 5 kHz (Fig. 5). In future work, dc signals could be upmodulated to this low-noise band using an ac bias field.

VI. DISCUSSION

At present, the MW source's phase noise is the dominant noise source. Calculations suggest removing this contribution would allow a sensitivity of $4.8 \text{ pT}/\sqrt{\text{Hz}}$ (see Sec. S10 in the Supplemental Material [62]). Although using a MW source with better phase noise is feasible, it may be similarly effective to use a Pound-type scheme [82], where the cavity is interrogated with a frequency-modulated signal. This encodes the reflected signal at the modulation frequency, where the MW source's phase noise can be substantially lower. In either case, improvements or changes to the remaining readout and MW electronics would then be required to approach the thermal-noise limit $\eta_{\text{th}} = 1.1 \text{ pT}/\sqrt{\text{Hz}}$ (see Sec. S10 in the Supplemental Material [62]).

To further improve device sensitivity, the thermal-noise limit must be decreased. Section S11 in the Supplemental Material [62] shows that while improving the resonator linewidth will produce little change in the thermal-noise limit, increasing the number of polarized spins or reducing the spin linewidth should be more effective. Using a whispering gallery mode in a physically larger resonator would likely increase the number of polarized spins as well as the optimal interrogation power [83–85]. On the other hand, the prospects for improving the spin linewidth in ruby remain unclear, as κ_s is likely limited by interactions between Cr^{3+} and ^{27}Al in the lattice, as detailed in Sec. S2 in the Supplemental Material [62].

Other changes might improve the sensor's flexibility or utility. Presently, a field of approximately 0.003 T ensures the $|m_s = \pm \frac{1}{2}\rangle$ and $|m_s = \pm \frac{3}{2}\rangle$ spin states are well resolved spectroscopically and the resonator strongly couples only to a single spin transition. For applications requiring accurate measurement of low-frequency or dc fields, drift in this bias field could be problematic. An alternative approach might resolve the desired transition using circularly polarized microwaves instead, thus removing the requirement for any bias field. With a bias field, the magnetometer acts as a vector sensor (see Sec. S1 in the Supplemental Material [62]), but the device response without a bias field is more complicated, and further study is required to develop a scheme for vector magnetometry using circularly polarized probe microwaves.

This work demonstrates a generalization of the MW cavity readout technique [38] combined with spin states prepared by thermal spin polarization arising from a ZFS. By removing the need for optical polarization, solid-state spin sensors can be made smaller, lighter, and more power efficient, as well as avoid challenges of light delivery, including high heat loads and laser pointing, polarization,

and amplitude noise. Further, this technique is applicable to a broad class of paramagnetic defects, including those with a ZFS at gigahertz scale or higher. As a result, paramagnetic defects which are currently unsuitable for sensors due to poor optical initialization or poor optical readout may become viable. For example, the approach demonstrated here could be further developed as an alternative readout scheme for silicon vacancies or divacancies in SiC [86–89]. Access to a broader range of defects may offer a variety of advantages, including improved performance due to application-tailored energy-level structures, material loss tangents, and dielectric constants. In addition, the use of alternative defects could spur advances in sensing modalities beyond magnetometry, including electric field and time sensing [90].

-
- [1] M. Karadas, A. M. Wojciechowski, A. Huck, N. O. Dalby, U. L. Andersen, and A. Thielscher, Feasibility and resolution limits of opto-magnetic imaging of neural network activity in brain slices using color centers in diamond, *Sci. Rep.* **8**, 1 (2018).
 - [2] F. M. Stürner, A. Brenneis, T. Buck, J. Kassel, R. Rölver, T. Fuchs, A. Savitsky, D. Suter, J. Grimmel, S. Hengesbach, M. Förtsch, K. Nakamura, H. Sumiya, S. Onoda, J. Isoya, and F. Jelezko, Integrated and portable magnetometer based on nitrogen-vacancy ensembles in diamond, *Adv. Quantum Technol.* **4**, 2000111 (2021).
 - [3] J. F. Barry, M. J. Turner, J. M. Schloss, D. R. Glenn, Y. Song, M. D. Lukin, H. Park, and R. L. Walsworth, Optical magnetic detection of single-neuron action potentials using quantum defects in diamond, *Proc. Natl. Acad. Sci.* **113**, 14133 (2016).
 - [4] H. C. Davis, P. Ramesh, A. Bhatnagar, A. Lee-Gosselin, J. F. Barry, D. R. Glenn, R. L. Walsworth, and M. G. Shapiro, Mapping the microscale origins of magnetic resonance image contrast with subcellular diamond magnetometry, *Nat. Commun.* **9**, 131 (2018).
 - [5] K. Arai, A. Kuwahata, D. Nishitani, I. Fujisaki, R. Matsuki, Z. Xin, Y. Nishio, X. Cao, Y. Hatano, S. Onoda, C. Shinei, M. Miyakawa, T. Taniguchi, M. Yamazaki, T. Teraji, T. Ohshima, M. Hatano, M. Sekino, and T. Iwasaki, Millimetre-scale magnetocardiography of living rats using a solid-state quantum sensor, (2021), [ArXiv:2105.11676](https://arxiv.org/abs/2105.11676).
 - [6] J. L. Webb, L. Troise, N. W. Hansen, C. Olsson, A. M. Wojciechowski, J. Achard, O. Brinza, R. Staacke, M. Kieschnick, J. Meijer, A. Thielscher, J.-F. Perrier, K. Berg-Sørensen, A. Huck, and U. L. Andersen, Detection of biological signals from a live mammalian muscle using an early stage diamond quantum sensor, *Sci. Rep.* **11**, 2412 (2021).
 - [7] I. Fescenko, A. Laraoui, J. Smits, N. Mosavian, P. Kehayias, J. Seto, L. Bougas, A. Jarmola, and V. M. Acosta, Diamond Magnetic Microscopy of Malarial Hemozoin Nanocrystals, *Phys. Rev. Appl.* **11**, 034029 (2019).
 - [8] F. Shi, Q. Zhang, P. Wang, H. Sun, J. Wang, X. Rong, M. Chen, C. Ju, F. Reinhard, H. Chen, J. Wrachtrup, J. Wang,

- and J. Du, Single-protein spin resonance spectroscopy under ambient conditions, *Science* **347**, 1135 (2015).
- [9] L. Q. Zhou, R. L. Patel, A. C. Frangeskou, A. Nikitin, B. L. Green, B. G. Breeze, S. Onoda, J. Isoya, and G. W. Morley, Imaging Damage in Steel Using a Diamond Magnetometer, *Phys. Rev. Appl.* **15**, 024015 (2021).
- [10] M. J. Turner, N. Langellier, R. Bainbridge, D. Walters, S. Meesala, T. M. Babinec, P. Kehayias, A. Yacoby, E. Hu, M. Lončar, R. L. Walsworth, and E. V. Levine, Magnetic Field Fingerprinting of Integrated-Circuit Activity with a Quantum Diamond Microscope, *Phys. Rev. Appl.* **14**, 014097 (2020).
- [11] R. Patel, L. Zhou, A. Frangeskou, G. Stimpson, B. Breeze, A. Nikitin, M. Dale, E. Nichols, W. Thornley, B. Green, M. Newton, A. Edmonds, M. Markham, D. Twitchen, and G. Morley, Subnanotesla Magnetometry with a Fiber-Coupled Diamond Sensor, *Phys. Rev. Appl.* **14**, 044058 (2020).
- [12] I. Bertelli, J. J. Carmiggelt, T. Yu, B. G. Simon, C. C. Pothoven, G. E. W. Bauer, Y. M. Blanter, J. Aarts, and T. van der Sar, Magnetic resonance imaging of spin-wave transport and interference in a magnetic insulator, *Sci. Adv.* **6**, eabd3556 (2020).
- [13] T. Lenz, G. Chatzidrosos, Z. Wang, L. Bougas, Y. Dumeige, A. Wickenbrock, N. Kerber, J. Zázvorka, F. Kammerbauer, and M. Kläui, *et al.*, Imaging Topological Spin Structures Using Light-Polarization and Magnetic Microscopy, *Phys. Rev. Appl.* **15**, 024040 (2021).
- [14] A. Jenkins, S. Baumann, H. Zhou, S. A. Meynell, D. Yang, K. Watanabe, T. Taniguchi, A. Lucas, A. F. Young, and A. C. Bleszynski Jayich, Imaging the breakdown of ohmic transport in graphene, (2020), *ArXiv:2002.05065*.
- [15] S. Hsieh, P. Bhattacharyya, C. Zu, T. Mittiga, T. J. Smart, F. Machado, B. Kobrin, T. O. Höhn, N. Z. Rui, M. Kamrani, S. Chatterjee, S. Choi, M. Zaletel, V. V. Struzhkin, J. E. Moore, V. I. Levitas, R. Jeanloz, and N. Y. Yao, Imaging stress and magnetism at high pressures using a nanoscale quantum sensor, *Science* **366**, 1349 (2019).
- [16] I. Lovchinsky, A. O. Sushkov, E. Urbach, N. P. de Leon, S. Choi, K. De Greve, R. Evans, R. Gertner, E. Bersin, C. Müller, L. McGuinness, F. Jelezko, R. L. Walsworth, H. Park, and M. D. Lukin, Nuclear magnetic resonance detection and spectroscopy of single proteins using quantum logic, *Science* **351**, 836 (2016).
- [17] J. Achard, V. Jacques, and A. Tallaire, Chemical vapour deposition diamond single crystals with nitrogen-vacancy centres: A review of material synthesis and technology for quantum sensing applications, *J. Phys. D: Appl. Phys.* **53**, 313001 (2020).
- [18] A. Tallaire, O. Brinza, P. Huillery, T. Delord, C. Pellet-Mary, R. Staacke, B. Abel, S. Pezzagna, J. Meijer, N. Touati, L. Binet, A. Ferrier, P. Goldner, G. Hetet, and J. Achard, High NV density in a pink CVD diamond grown with N₂O addition, *Carbon* **170**, 421 (2020).
- [19] S. T. Alsid, J. F. Barry, L. M. Pham, J. M. Schloss, M. F. O’Keeffe, P. Cappellaro, and D. A. Braje, Photoluminescence Decomposition Analysis: A Technique to Characterize N-V Creation in Diamond, *Phys. Rev. Appl.* **12**, 044003 (2019).
- [20] M. N. Ashfold, J. P. Goss, B. L. Green, P. W. May, M. E. Newton, and C. V. Peaker, Nitrogen in diamond, *Chem. Rev.* **120**, 5745 (2020).
- [21] E. Bauch, S. Singh, J. Lee, C. A. Hart, J. M. Schloss, M. J. Turner, J. F. Barry, L. M. Pham, N. Bar-Gill, S. F. Yelin, and R. L. Walsworth, Decoherence of ensembles of nitrogen-vacancy centers in diamond, *Phys. Rev. B* **102**, 134210 (2020).
- [22] G. Wolfowicz, F. J. Heremans, C. P. Anderson, S. Kanai, H. Seo, A. Gali, G. Galli, and D. D. Awschalom, Quantum guidelines for solid-state spin defects, *Nat. Rev. Mater.* (2021).
- [23] A. M. Edmonds, C. A. Hart, M. J. Turner, P.-O. Colard, J. M. Schloss, K. Olsson, R. Trubko, M. L. Markham, A. Rathmill, B. Horne-Smith, W. Lew, A. Manickam, S. Bruce, P. G. Kaup, J. C. Russo, M. J. DiMario, J. T. South, J. T. Hansen, D. J. Twitchen, and R. Walsworth, Characterisation of CVD diamond with high concentrations of nitrogen for magnetic-field sensing applications, *Mater. Quantum Technol.* **1**, 025001 (2021).
- [24] A. Watanabe, T. Nishikawa, H. Kato, M. Fujie, M. Fujiwara, T. Makino, S. Yamasaki, E. Herbschleb, and N. Mizuochi, Shallow NV centers augmented by exploiting n-type diamond, *Carbon* **178**, 294 (2021).
- [25] D. Bluvstein, Z. Zhang, and A. C. B. Jayich, Identifying and Mitigating Charge Instabilities in Shallow Diamond Nitrogen-Vacancy Centers, *Phys. Rev. Lett.* **122**, 076101 (2019).
- [26] N. Aslam, M. Pfender, P. Neumann, R. Reuter, A. Zappe, F. Fávoro de Oliveira, A. Denisenko, H. Sumiya, S. Onoda, J. Isoya, and J. Wrachtrup, Nanoscale nuclear magnetic resonance with chemical resolution, *Science* **357**, 67 (2017).
- [27] A. Waeber, G. Gillard, G. Ragunathan, M. Hopkinson, P. Spencer, D. Ritchie, M. Skolnick, and E. Chekhovich, Pulse control protocols for preserving coherence in dipolar-coupled nuclear spin baths, *Nat. Commun.* **10**, 3157 (2019).
- [28] M. F. O’Keeffe, L. Horesh, J. F. Barry, D. A. Braje, and I. L. Chuang, Hamiltonian engineering with constrained optimization for quantum sensing and control, *New J. Phys.* **21**, 023015 (2019).
- [29] D. R. Glenn, D. B. Bucher, J. Lee, M. D. Lukin, H. Park, and R. L. Walsworth, High-resolution magnetic resonance spectroscopy using a solid-state spin sensor, *Nature* **555**, 351 (2018).
- [30] E. Bauch, C. A. Hart, J. M. Schloss, M. J. Turner, J. F. Barry, P. Kehayias, S. Singh, and R. L. Walsworth, Ultralong Dephasing Times in Solid-State Spin Ensembles via Quantum Control, *Phys. Rev. X* **8**, 031025 (2018).
- [31] J. Smits, J. T. Damron, P. Kehayias, A. F. McDowell, N. Mosavian, I. Fescenko, N. Ristoff, A. Laraoui, A. Jarmola, and V. M. Acosta, Two-dimensional nuclear magnetic resonance spectroscopy with a microfluidic diamond quantum sensor, *Sci. Adv.* **5**, eaaw7895 (2019).
- [32] N. Bar-Gill, L. M. Pham, A. Jarmola, D. Budker, and R. L. Walsworth, Solid-state electronic spin coherence time approaching one second, *Nat. Commun.* **4**, 1743 (2013).

- [33] A. Dréau, M. Lesik, L. Rondin, P. Spinicelli, O. Arcizet, J.-F. Roch, and V. Jacques, Avoiding power broadening in optically detected magnetic resonance of single NV defects for enhanced dc magnetic field sensitivity, *Phys. Rev. B* **84**, 195204 (2011).
- [34] C. A. Hart, J. M. Schloss, M. J. Turner, P. J. Scheidegger, E. Bauch, and R. L. Walsworth, N- V -diamond Magnetic Microscopy Using a Double Quantum 4-Ramsey Protocol, *Phys. Rev. Appl.* **15**, 044020 (2021).
- [35] L. M. Pham, N. Bar-Gill, C. Belthangady, D. Le Sage, P. Cappellaro, M. D. Lukin, A. Yacoby, and R. L. Walsworth, Enhanced solid-state multispin metrology using dynamical decoupling, *Phys. Rev. B* **86**, 045214 (2012).
- [36] P. Neumann, J. Beck, M. Steiner, F. Rempp, H. Fedder, P. R. Hemmer, J. Wrachtrup, and F. Jelezko, Single-shot readout of a single nuclear spin, *Science* **329**, 542 (2010).
- [37] B. J. Shields, Q. P. Unterreithmeier, N. P. de Leon, H. Park, and M. D. Lukin, Efficient Readout of a Single Spin State in Diamond via Spin-To-Charge Conversion, *Phys. Rev. Lett.* **114**, 136402 (2015).
- [38] E. R. Eisenach, J. F. Barry, M. F. O’Keeffe, J. M. Schloss, M. H. Steinecker, D. R. Englund, and D. A. Braje, Cavity-enhanced microwave readout of a solid-state spin sensor, *Nat. Commun.* **12**, 1357 (2021).
- [39] J. Ebel, T. Joas, M. Schalk, P. Weinbrenner, A. Angerer, J. Majer, and F. Reinhard, Dispersive readout of room-temperature ensemble spin sensors, *Quantum Sci. Technol.* **6**, 03LT01 (2021).
- [40] E. Bourgeois, A. Jarmola, P. Siyushev, M. Gulka, J. Hruby, F. Jelezko, D. Budker, and M. Nesladek, Photoelectric detection of electron spin resonance of nitrogen-vacancy centres in diamond, *Nat. Commun.* **6**, 1 (2015).
- [41] D. A. Hopper, R. R. Grote, A. L. Exarhos, and L. C. Bassett, Near-infrared-assisted charge control and spin readout of the nitrogen-vacancy center in diamond, *Phys. Rev. B* **94**, 241201 (2016).
- [42] D. A. Hopper, H. J. Shulevitz, and L. C. Bassett, Spin readout techniques of the nitrogen-vacancy center in diamond, *Micromachines* **9**, 437 (2018).
- [43] M. Niethammer, M. Widmann, T. Rendler, N. Morioka, Y.-C. Chen, R. Stöhr, J. U. Hassan, S. Onoda, T. Ohshima, S.-Y. Lee, A. Mukherjee, J. Isoya, N. T. Son, and J. Wrachtrup, Coherent electrical readout of defect spins in silicon carbide by photo-ionization at ambient conditions, *Nat. Commun.* **10**, 5569 (2019).
- [44] J. F. Barry, J. M. Schloss, E. Bauch, M. J. Turner, C. A. Hart, L. M. Pham, and R. L. Walsworth, Sensitivity optimization for NV-diamond magnetometry, *Rev. Mod. Phys.* **92**, 015004 (2020).
- [45] P. Kehayias, A. Jarmola, N. Mosavian, I. Fescenko, F. M. Benito, A. Laraoui, J. Smits, L. Bougas, D. Budker, A. Neumann, S. R. J. Brueck, and V. M. Acosta, Solution nuclear magnetic resonance spectroscopy on a nanostructured diamond chip, *Nat. Commun.* **8**, 188 (2017).
- [46] I. Fescenko, A. Jarmola, I. Savukov, P. Kehayias, J. Smits, J. Damron, N. Ristoff, N. Mosavian, and V. M. Acosta, Diamond magnetometer enhanced by ferrite flux concentrators, *Phys. Rev. Res.* **2**, 023394 (2020).
- [47] D. B. Bucher, D. R. Glenn, H. Park, M. D. Lukin, and R. L. Walsworth, Hyperpolarization-Enhanced NMR Spectroscopy with Femtomole Sensitivity Using Quantum Defects in Diamond, *Phys. Rev. X* **10**, 021053 (2020).
- [48] K.-M. C. Fu, G. Z. Iwata, A. Wickenbrock, and D. Budker, Sensitive magnetometry in challenging environments, *AVS Quantum Sci.* **2**, 044702 (2020).
- [49] C. L. Degen, F. Reinhard, and P. Cappellaro, Quantum sensing, *Rev. Mod. Phys.* **89**, 035002 (2017).
- [50] R. C. Jaklevic, J. Lambe, A. H. Silver, and J. E. Mercereau, Quantum Interference Effects in Josephson Tunneling, *Phys. Rev. Lett.* **12**, 159 (1964).
- [51] I. K. Kominis, T. W. Kornack, J. C. Allred, and M. V. Romalis, A subfemtotesla multichannel atomic magnetometer, *Nature* **422**, 596 (2003).
- [52] A. Grosz, G. Haji-Sheikh, and S. Mukhopadhyay, *High Sensitivity Magnetometers* (Springer, 2017).
- [53] J. M. Taylor, P. Cappellaro, L. Childress, L. Jiang, D. Budker, P. R. Hemmer, A. Yacoby, R. Walsworth, and M. D. Lukin, High-sensitivity diamond magnetometer with nanoscale resolution, *Nat. Phys.* **4**, 810 (2008).
- [54] G. Kucsko, P. C. Maurer, N. Y. Yao, M. Kubo, H. J. Noh, P. K. Lo, H. Park, and M. D. Lukin, Nanometre-scale thermometry in a living cell, *Nature* **500**, 54 (2013).
- [55] P. Neumann, I. Jakobi, F. Dolde, C. Burk, R. Reuter, G. Waldherr, J. Honert, T. Wolf, A. Brunner, J. H. Shim, D. Suter, H. Sumiya, J. Isoya, and J. Wrachtrup, High-precision nanoscale temperature sensing using single defects in diamond, *Nano Lett.* **13**, 2738 (2013).
- [56] S.-C. Zhang, Y. Dong, B. Du, H.-B. Lin, S. Li, W. Zhu, G.-Z. Wang, X.-D. Chen, G.-C. Guo, and F.-W. Sun, A robust fiber-based quantum thermometer coupled with nitrogen-vacancy centers, *Rev. Sci. Instrum.* **92**, 044904 (2021).
- [57] Y. Nishimura, K. Oshimi, Y. Umehara, Y. Kumon, K. Miyaji, H. Yukawa, Y. Shikano, T. Matsubara, M. Fujiwara, Y. Baba, and Y. Teki, Wide-field fluorescent nanodiamond spin measurements toward real-time large-area intracellular thermometry, *Sci. Rep.* **11**, 4248 (2021).
- [58] J. Michl, J. Steiner, A. Denisenko, A. Bülau, A. Zimmermann, K. Nakamura, H. Sumiya, S. Onoda, P. Neumann, J. Isoya, and J. Wrachtrup, Robust and accurate electric field sensing with solid state spin ensembles, *Nano Lett.* **19**, 4904 (2019).
- [59] B. Yang, T. Murooka, K. Mizuno, K. Kim, H. Kato, T. Makino, M. Ogura, S. Yamasaki, M. E. Schmidt, H. Mizuta, A. Yacoby, M. Hatano, and T. Iwasaki, Vector Electrometry in a Wide-Gap-Semiconductor Device Using a Spin-Ensemble Quantum Sensor, *Phys. Rev. Appl.* **14**, 044049 (2020).
- [60] E. H. Chen, H. A. Clevenson, K. A. Johnson, L. M. Pham, D. R. Englund, P. R. Hemmer, and D. A. Braje, High-sensitivity spin-based electrometry with an ensemble of nitrogen-vacancy centers in diamond, *Phys. Rev. A* **95**, 053417 (2017).
- [61] T.-T. Chang, D. Foster, A. H. Kahn, An intensity standard for electron paramagnetic resonance using chromium-doped corundum ($\text{Al}_2\text{O}_3 : \text{Cr}^{3+}$), *J. Res. Natl. Bur. Stand.* **83**, 133 (1978).
- [62] See Supplemental Material at <http://link.aps.org/supplemental/10.1103/PhysRevApplied.17.044004> for more

- information on ruby properties, power and magnetic field calibration, parameter estimation, and noise analysis, which includes the Refs. [93–107].
- [63] C. P. Poole, *Electron Spin Resonance: A Comprehensive Treatise on Experimental Techniques* (Dover Publications, Inc., Mineola, New York, 1996).
- [64] J. H. N. Loubser and J. A. van Wyk, Electron spin resonance in the study of diamond, *Rep. Prog. Phys.* **41**, 1201 (1978).
- [65] G. R. Eaton, S. S. Eaton, D. P. Barr, and R. T. Weber, *Quantitative EPR* (Springer Science & Business Media, Vienna, 2010).
- [66] R. Cammack, in *Encyclopedia of Biophysics*, edited by G. C. K. Roberts (Springer Berlin Heidelberg, Berlin, Heidelberg, 2013), p. 695.
- [67] D. G. Blair and I. N. Evans, High-Q microwave properties of a sapphire ring resonator, *J. Phys. D: Appl. Phys.* **15**, 1651 (1982).
- [68] D. C. Harris, in *Window and Dome Technologies VIII*, Vol. 5078, edited by R. W. Tustison, International Society for Optics and Photonics (SPIE, 2003), p. 1.
- [69] V. Kurlov, in *Reference Module in Materials Science and Materials Engineering* (Elsevier, 2016).
- [70] V. K. Sewani, R. J. Stöhr, R. Kolesov, H. H. Vallabhapurapu, T. Simmet, A. Morello, and A. Laucht, Spin thermometry and spin relaxation of optically detected Cr^{3+} ions in ruby Al_2O_3 , *Phys. Rev. B* **102**, 104114 (2020).
- [71] J. D. Breeze, E. Salvadori, J. Sathian, N. M. Alford, and C. W. Kay, Room-temperature cavity quantum electrodynamics with strongly coupled dicke states, *npj Quantum Inf.* **3**, 40 (2017).
- [72] J. D. Breeze, E. Salvadori, J. Sathian, N. M. Alford, and C. W. Kay, Continuous-wave room-temperature diamond maser, *Nature* **555**, 493 (2018).
- [73] J. Breeze, *Temperature and Frequency Dependence of Complex Permittivity in Metal Oxide Dielectrics: Theory, Modelling and Measurement* (Springer, 2016).
- [74] J. Krupka, K. Derzakowski, M. Tobar, J. Harnett, and R. G. Geyer, Complex permittivity of some ultralow loss dielectric crystals at cryogenic temperatures, *Meas. Sci. Technol.* **10**, 387 (1999).
- [75] Y. Kobayashi and T. Senju, Resonant modes in shielded uniaxial-anisotropic dielectric rod resonators, *IEEE Trans. Microwave Theory Tech.* **41**, 2198 (1993).
- [76] Without the SiC, which lowers the quality-factor due to a higher loss tangent [74,91] and spreading of the mode, we measured $Q_0 = 50\,000$.
- [77] M. E. Tobar, J. Krupka, E. N. Ivanov, and R. A. Woode, in *Proceedings of 1996 IEEE International Frequency Control Symposium* (1996), p. 799.
- [78] The spin resonance has an observed linewidth $\kappa_s = 2\pi \times 42\text{MHz}$, corresponding to 15 G. Thus, for bias magnetic fields greater than approximately 15 G, the $|m_s = +\frac{1}{2}\rangle \leftrightarrow |m_s = +\frac{3}{2}\rangle$ transition is spectrally separated from all other transitions.
- [79] The low-noise amplifier is removed from the signal chain during this process to reduce amplitude-dependent distortion on the reflected signal.
- [80] H. Tanji-Suzuki, I. D. Leroux, M. H. Schleier-Smith, M. Cetina, A. T. Grier, J. Simon, and V. Vuletić, in *Advances in Atomic, Molecular, and Optical Physics*, Vol. 60, edited by E. Arimondo, P. Berman, and C. Lin (Academic Press, 2011), p. 201.
- [81] A. Abragam, *Principles of Nuclear Magnetism*, International Series of Monographs on Physics (Clarendon Press, 1983).
- [82] R. V. Pound, Electronic frequency stabilization of microwave oscillators, *Rev. Sci. Instrum.* **17**, 490 (1946).
- [83] W. G. Farr, M. Goryachev, D. L. Creedon, and M. E. Tobar, Strong coupling between whispering gallery modes and chromium ions in ruby, *Phys. Rev. B* **90**, 054409 (2014).
- [84] J. Bourhill, M. Goryachev, W. G. Farr, and M. E. Tobar, Collective behavior of Cr^{3+} ions in ruby revealed by whispering gallery modes, *Phys. Rev. A* **92**, 023805 (2015).
- [85] W. G. Farr, D. L. Creedon, M. Goryachev, K. Benmesai, and M. E. Tobar, Ultrasensitive microwave spectroscopy of paramagnetic impurities in sapphire crystals at millikelvin temperatures, *Phys. Rev. B* **88**, 224426 (2013).
- [86] D. Simin, F. Fuchs, H. Kraus, A. Sperlich, P. G. Baranov, G. V. Astakhov, and V. Dyakonov, High-Precision Angle-Resolved Magnetometry with Uniaxial Quantum Centers in Silicon Carbide, *Phys. Rev. Appl.* **4**, 014009 (2015).
- [87] H. Kraus, V. Soltamov, D. Riedel, S. Vāth, F. Fuchs, A. Sperlich, P. Baranov, V. Dyakonov, and G. Astakhov, Room-temperature quantum microwave emitters based on spin defects in silicon carbide, *Nat. Phys.* **10**, 157 (2014).
- [88] M. Niethammer, M. Widmann, S.-Y. Lee, P. Stenberg, O. Kordina, T. Ohshima, N. T. Son, E. Janzén, and J. Wrachtrup, Vector Magnetometry Using Silicon Vacancies in 4H-SiC under Ambient Conditions, *Phys. Rev. Appl.* **6**, 034001 (2016).
- [89] J. B. S. Abraham, C. Gutzsell, D. Todorovski, S. Sperling, J. E. Epstein, B. S. Tien-Street, T. M. Sweeney, J. J. Wathen, E. A. Pogue, P. G. Brereton, T. M. McQueen, W. Frey, B. D. Clader, and R. Osiander, Nanoscale Magnetometry with the Silicon Vacancy in Silicon Carbide, *Phys. Rev. Appl.* **15**, 064022 (2021).
- [90] M. E. Trusheim, K. Jacobs, J. E. Hoffman, D. P. Fahey, D. A. Braje, and D. Englund, A polariton-stabilized spin clock, (2020), [ArXiv:2009.02427](https://arxiv.org/abs/2009.02427).
- [91] V. Parshin, E. Serov, G. Denisov, B. Garin, R. Denisyuk, V. V'yuginov, V. Klevtsov, and N. Travin, Silicon carbide for high-power applications at MM and THz ranges, *Diamond Relat. Mater.* **80**, 1 (2017).
- [92] E. O. Schulz-Du Bois, Paramagnetic spectra of substituted sapphires - part I: Ruby, *Bell Sys. Tech. J.* **38**, 271 (1959).
- [93] W. J. C. Grant and M. W. P. Strandberg, Line shapes of paramagnetic resonances of chromium in ruby, *Phys. Rev.* **135**, A727 (1964).
- [94] R. F. Wenzel, Second moment of the Cr^{3+} EPR line in ruby broadened by strong hyperfine interactions, *Phys. Rev. B* **1**, 3109 (1970).
- [95] S. A. Peskovatskii, Electromultipole interaction and paramagnetic relaxation in ruby I. EPR line shape in ruby, *Phys. Stat. Sol.* **40**, 347 (1970).
- [96] R. Boscaino, M. Brai, I. Ciccarello, and G. Contrino, Line broadening of the EPR absorption spectrum of ruby, *Phys. Lett. A* **46**, 190 (1973).

- [97] A. Szabo, T. Muramoto, and R. Kaarli, ^{27}Al nuclear-spin dephasing in the ruby frozen core and Cr^{3+} spin-flip-time measurements, *Phys. Rev. B* **42**, 7769 (1990).
- [98] A. M. Portis, Electronic structure of F centers: Saturation of the electron spin resonance, *Phys. Rev.* **91**, 1071 (1953).
- [99] C. P. Poole and H. A. Farach, Line shapes in electron spin resonance, *Bull. Magn. Reson.* **1**, 162 (1979).
- [100] A. A. Manenkov and A. M. Prokhorov, Spin-lattice relaxation in chromium corundum, *Sov. Phys. JETP* **11**, 3 (1960).
- [101] J. A. Giordmaine, L. E. Alsop, F. R. Nash, and C. H. Townes, Paramagnetic relaxation at very low temperatures, *Phys. Rev.* **109**, 302 (1958).
- [102] D. I. Schuster, A. P. Sears, E. Ginossar, L. DiCarlo, L. Frunzio, J. J. L. Morton, H. Wu, G. A. D. Briggs, B. B. Buckley, D. D. Awschalom, and R. J. Schoelkopf, High-Cooperativity Coupling of Electron-Spin Ensembles to Superconducting Cavities, *Phys. Rev. Lett.* **105**, 140501 (2010).
- [103] P. Villars, K. Cenzual, eds., *PAULING FILE in: Inorganic Solid Phases*, SpringerMaterials (online database) (Springer, Heidelberg, SpringerMaterials, 2016).
- [104] D. Meeker, Finite element method magnetics (2019).
- [105] J. P. Van Der Ziel and N. Bloembergen, Optically induced magnetization in ruby, *Phys. Rev.* **138**, A1287 (1965).
- [106] R. Michel, The temperature-dependence of electron spin-lattice relaxation times in ruby, *J. Phys. Chem. Solids* **13**, 164 (1960).
- [107] C. M. Verber, H. P. Mahon, and W. H. Tanttilla, Nuclear resonance of aluminum in synthetic ruby, *Phys. Rev.* **125**, 1149 (1962).